ELSEVIER

Contents lists available at ScienceDirect

# Journal of Solid State Chemistry

journal homepage: www.elsevier.com/locate/jssc





# Structure and redox properties of CeMnO<sub>3</sub> thin films

Kai Shen <sup>a</sup>, Mengjie Fan <sup>a</sup>, Rajeev Kumar Rai <sup>b</sup>, Eric A. Stach <sup>b</sup>, Raymond J. Gorte <sup>a</sup>, John M. Vohs <sup>a</sup>, <sup>\*</sup>

- <sup>a</sup> Department of Chemical and Biomolecular Engineering, University of Pennsylvania, Philadelphia, PA, 19104, USA
- b Department of Materials Science and Engineering, University of Pennsylvania, Philadelphia, PA, 19104, USA

#### ARTICLE INFO

Keywords:
Perovskite
Fluorite
CeMnO<sub>3</sub>
Synthesis
Thin film
Reversible phase transition

#### ABSTRACT

Conformal thin films of a cerium-manganese mixed oxide with a stoichiometry of CeMnO $_{\rm x}$  were deposited on a high-surface-area  $\gamma$ -Al $_2$ O $_3$  support by Atomic Layer Deposition (ALD). Upon redox cycling, the CeMnO $_{\rm x}$  film underwent a reversible phase transition between a reduced perovskite CeMnO $_3$  phase and an oxidized fluorite CeMnO $_{3.5}$  phase, as shown by X-ray diffraction (XRD) and High-Resolution Scanning/Transmission Electron Microscopy (HR-S/TEM). X-ray Photoelectron Spectroscopy (XPS) and Electron Energy Loss Spectroscopy (EELS) revealed that Ce and Mn were in +3-oxidation states in the reduced perovskite phase and +4 and + 3 respectively in the oxidized fluorite phase. The composition of the film as a function of P(O $_2$ ) at 1073 K was measured by coulometric titration and showed that a transition between Ce $_3$ <sup>+</sup> and Ce $_4$ <sup>+</sup> occurred at a P(O $_2$ ) of 10<sup>-9</sup> atm, a value that is much higher than that required for oxidizing either reduced bulk ceria or thin-film ceria on  $_7$ -Al $_2$ O $_3$ . These properties make CeMnO $_8$  films an interesting candidate for various catalytic applications.

# 1. Introduction

Ceria (CeO<sub>2</sub>) is a crucial component in automotive three-way catalysts due to its ability to store and release oxygen [1]. Because well-crystallized, bulk ceria is not easily reduced [2], three-way catalysts use a more reducible, mixed ceria-zirconia, solid solution [3,4]. When doped with  $\mathrm{Gd}^{3+}$  or  $\mathrm{Sm}^{3+}$ , ceria is also an important oxygen-ion conductor [5]. In both of these applications, the mixed oxides form a single phase, with all of the metal cations existing within a fluorite lattice when fully oxidized.

The ability to tune the properties of ceria by mixing with a second oxide has driven an interest in other ceria-mixed oxides [6,7], especially mixtures with other catalytically active oxides, such as  $Fe_2O_3$ ,  $Mn_2O_3$ , and  $V_2O_5$ . Since these other oxides do not exist in a fluorite structure, there is a question of whether single-phase oxides can be formed and what structure they would take. With  $V_2O_5$ , the compound oxide,  $CeVO_4$ , and its reduced analog,  $CeVO_3$ , are well known and very stable, with  $CeVO_4$  and  $CeVO_3$  having zircon and perovskite structures, respectively [8]. Interestingly, Ce is in the +3-oxidation state in both of these structures and cannot be oxidized to  $Ce^{+4}$ , even in the presence of an oxygen plasma [9]. With  $Fe_2O_3$ , it is possible to form a perovskite,  $CeFeO_3$  phase under highly reducing conditions [10]; however, it is not clear whether a single-phase mixed oxide can form under oxidizing

conditions. In a recent investigation from our laboratories [11], bulk CeFeO<sub>3</sub> appeared to irreversibly separate into a physical mixture of the individual components upon high-temperature oxidation.

Although there have been claims that Mn cations can dope the  $CeO_2$  fluorite lattice [12–15], the evidence for the formation of a single-phase mixed oxide was primarily the lack of additional peaks in x-ray diffraction (XRD). Since XRD cannot detect amorphous phases, this is not conclusive. Indeed, at least one study of  $CeO_2$ –Mn $_2O_3$  mixtures that showed only a fluorite phase in XRD concluded that the material was just a physical mixture based on the absence of a shift in the XRD lattice parameter from that of pure  $CeO_2$  and on thermodynamic, redox measurements which were identical to what would be expected for a physical mixture of  $CeO_2$  and  $Mn_2O_3$  [16]. Another study that attempted to prepare a  $CeMnO_3$  perovskite under reducing conditions concluded that this material was not stable [17].

Our laboratories recently studied thin films of CeFeO $_x$ , on  $\gamma$ -Al $_2O_3$  prepared by Atomic Layer Deposition (ALD) and found that the mixed oxides could reversibly transition from a fluorite phase under oxidizing conditions to a perovskite phase under reducing conditions [11]. We concluded that the thin-film morphology and interactions with the  $\gamma$ -Al $_2O_3$  support prevented the separation of cations into their pure component phases. Under reducing conditions, the intrinsic stability of the perovskite structure brought the cations together to form CeFeO $_3$ .

E-mail address: vohs@seas.upenn.edu (J.M. Vohs).

<sup>\*</sup> Corresponding author.

Because only a fluorite phase and nothing that could be related to  ${\rm FeO_x}$  was observed upon oxidation, it was suggested that the  ${\rm Fe^{+3}}$  cations were either in the lattice or present in interstices within the  ${\rm CeO_2}$  structure.

In the present study, we expanded our investigations of ALD-synthesized thin films to the  $CeMnO_x$  system. Similar to  $CeFeO_x$ , the thin films of  $CeMnO_x$  are shown to undergo a reversible transition from a fluorite phase following oxidation to a perovskite phase upon reduction. Also similar to what was found with  $CeFeO_x$ , it is the Ce that undergoes reduction from  $Ce^{+4}$  to  $Ce^{+3}$ , while the Mn remains in the +3-oxidation state. Potential applications for this material are also discussed.

# 2. Experimental section

#### 2.1. Sample preparation

The γ-Al<sub>2</sub>O<sub>3</sub> support (Strem Chemicals, Inc.) used in this study was calcined in air at 1173 K for 24 h, after which its Brunauer-Emmett-Teller (BET) specific surface area was 125 m<sup>2</sup> g<sup>-1</sup>. Cerium dioxide and manganese oxide were deposited onto the γ-Al<sub>2</sub>O<sub>3</sub> support using a homebuilt, vacuum, ALD apparatus that has been described in detail elsewhere [18]. The cerium and manganese precursors used in this study Tetrakis(2,2,6,6-tetramethyl-3,5-heptanedionato)cerium (TMHD)<sub>4</sub>, Strem Chemicals, Inc.) and Tris(2,2,6,6-tetramethyl-3, 5-heptanedionato)manganese (Mn(TMHD)<sub>3</sub>, Strem Chemicals, Inc.), respectively. Each ALD deposition cycle of Ce or Mn started by evacuating the γ-Al<sub>2</sub>O<sub>3</sub> support and then exposing it to a few Torr of the Ce or Mn precursor at 543 K for 5 min. After the exposure, excess precursor vapor was evacuated before the sample was subjected to oxidation in 1 atm air at 873 K for 5 min. Oxidation removed the ligands from the precursors and formed the corresponding metal oxide. The Ce and Mn growth rates were measured gravimetrically to be 3.9  $\times\,10^{13}$  Ce atoms·cm<sup>-2</sup>·cycle<sup>-1</sup> and  $4.7 \times 10^{13}$  Mn atoms·cm<sup>-2</sup>·cycle<sup>-1</sup>, respectively. To account for the different deposition rates, when growing the CeMnO<sub>x</sub> film, every five Mn ALD cycles were followed by six Ce ALD cycles to maintain a Ce:Fe molar ratio of 1:1. After a total of 65 Mn ALD cycles and 78 Ce ALD cycles and prior to any characterization studies, the sample was subjected to five redox cycles that consisted of reduction in 10% dry H<sub>2</sub> in He for 12 h, followed by oxidation in 10% dry air in He for 2 h at 1073 K.

#### 2.2. Characterization methods

BET specific surface areas were determined by measuring N2 adsorption isotherms at 78 K using a home-built apparatus. X-Ray Diffraction (XRD) patterns were acquired using a Rigaku MiniFlex diffractometer with a Cu-K $\alpha$  source ( $\lambda = 0.15416$  nm). High-resolution transmission electron microscopy (HRTEM), scanning transmission electron microscopy (STEM) and energy dispersive X-ray spectra (EDS) mappings were conducted on JEOL JEM-F200, operated at 200 kV. Electron energy-loss spectroscopy (EELS), along with STEM and EDS mappings, were obtained by an aberration-corrected JEOL NEOARM, operated at 200 kV in STEM mode. EELS was performed with a Gatan Image Filter which incorporates DualEELS capability to ensure accurate energy calibration and a K2-IS direct electron detector at the end of the filter. For ex-situ microscopy studies, the powder samples were diluted in ethanol and then deposited on a lacey carbon film on copper grids (Electron Microscopy Sciences, USA). X-Ray Photoelectron Spectra (XPS) were collected using an ultrahigh vacuum chamber equipped with a hemispherical electron energy analyzer (Leybold-Heraeus) and an Al-Kα X-ray source (VG Microtech). XPS spectra were fit using a Gaussian/ Lorentzian peaks with a Shirley-type background subtracted from each spectrum.

A home-built, Coulometric Titration (CT) apparatus was used to measure the oxygen stoichiometries for the  $CeMnO_X$  films as a function of  $P(O_2)$  at 1073 K (redox isotherm). The CT apparatus consisted of an

yttria-stabilized zirconia (YSZ) tube with Pt electrodes attached on its inner and outer surfaces [19]. Prior to the CT measurement, approximately 0.2 g of sample was placed in the middle of the tube and heated to 1073 K at a ramping rate of 1 K/min. A gas stream of  $3\%\,\rm H_2O$ ,  $10\%\,\rm H_2$  and  $87\%\,\rm He$  was passed through the YSZ tube for  $12\,\rm h$  to remove the air and create a  $\rm H_2O/H_2$  buffer in the gas phase to facilitate the measurement. After sealing both ends of the tube, a potentiostat (Gamry Instruments, Inc) was connected to the two Pt electrodes to monitor the Open-Circuit Voltage (OCV) across the electrodes, which in turn could be related to the  $\rm P(O_2)$  in the cell using the Nernst equation. The potentiostat could also apply a current between the two electrodes to pump oxygen into or out of the CT cell through the oxygen-ion conducting, YSZ tube. The total amount of oxygen added or removed from the cell was then determined from the charge passed through the YSZ membrane.

In addition to CT, flow titration was also used to measure the oxygen uptake by reduced samples. For these measurements, approximately 0.3 g of the sample was placed in a quartz tube, heated to 1073 K in flowing air (100 mL·min $^{-1}$ ), and then reduced in a flowing mixture of 10%  $\rm H_2$  in He at a total flowrate of 100 mL·min $^{-1}$  for 12 h. The sample was then oxidized in flowing 10% air in He while monitoring the effluent composition with a mass spectrometer (SRS RGA-100). The amount of  $\rm O_2$  consumed by the reduced sample during re-oxidation was determined by integrating the difference between the mass-spectrometer signals for oxygen and nitrogen.

#### 3. Results

#### 3.1. BET and XRD characterization

ALD was used to grow a film of CeMnO $_x$  on the  $\gamma$ -Al $_2$ O $_3$  support. Sufficient cycles were used to obtain 61 wt % loading of the oxide film which roughly corresponds to a thickness of 2 nm. This sample had a BET surface area of 38 m $^2$  g $^{-1}$  after being redox cycled 5 times at 1073 K; this value is one-third of that of the  $\gamma$ -Al $_2$ O $_3$  support (125 m $^2$  g $^{-1}$ ). This decrease in specific surface area was primarily due to the increase in mass upon film deposition, rather than from sintering of the sample.

The XRD patterns of the oxidized and reduced  $CeMnO_x/\gamma-Al_2O_3$  sample are presented in Fig. 1. The oxidized  $CeMnO_x/\gamma-Al_2O_3$  sample was exposed to 10% dry air in He for 2 h at 1073 K and then quenched to room temperature in the same gas flow prior to collecting the data. As labeled in the figure, the XRD pattern for this sample contain peaks

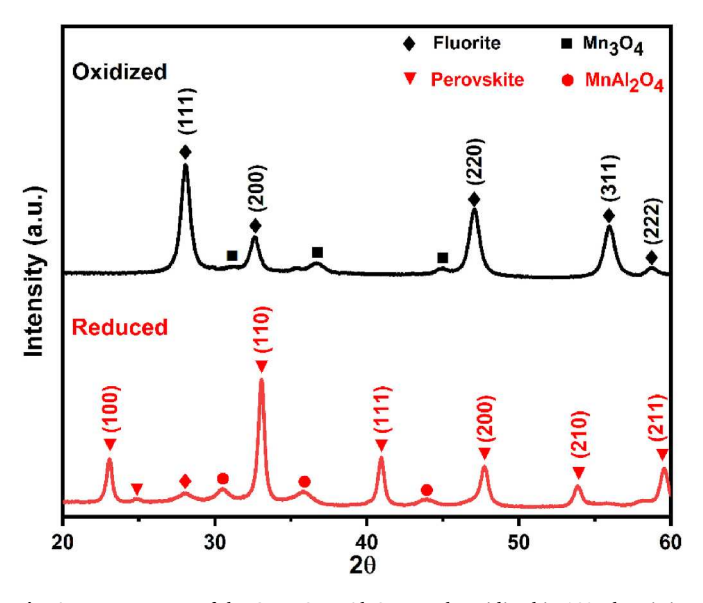


Fig. 1. XRD patterns of the  $CeMnO_x/\gamma$ - $Al_2O_3$  sample oxidized in 10% dry air in He (black) and reduced in 10% dry  $H_2$  in He (red) at 1073 K.

consistent with those expected for a fluorite crystal lattice. They are shifted by  $\sim\!0.5^\circ$  relative to that for fluorite  $\text{CeO}_2$  [20,21], which may be due to a change in lattice constant resulting from incorporation of some Mn cations into the lattice. A few small additional peaks between 30 and 50° 20 are also observed which can be assigned to Mn<sub>3</sub>O<sub>4</sub>. The intensities of these peaks, however, are too small to account for all the manganese in the sample, again suggesting that some of the Mn has been incorporated into the CeO<sub>2</sub> lattice. This scenario is consistent with that reported by Li et al. who characterized Mn-doped CeO<sub>2</sub> microspheres and showed that high levels of Mn could be doped into the lattice while maintaining the fluorite structure [22]. It is also possible, however, that at least some of the Mn is present in a second amorphous phase.

Significant changes in the XRD pattern were observed upon reducing the CeMnO $_{\rm x}/\gamma$ -Al $_{\rm 2}O_{\rm 3}$  sample in a stream of 10% dry H $_{\rm 2}$  in He for 12 h at 1073 K. After this treatment, prominent peaks at positions expected for a perovskite lattice were present in the XRD pattern. Much smaller peaks at positions consistent with MnAl $_{\rm 2}O_{\rm 4}$  were also observed, thus indicating that a small fraction of the Mn in the sample reacted with the  $\gamma$ -Al $_{\rm 2}O_{\rm 3}$  support. Even with the presence of these minor phases, the data indicates that the CeMnO $_{\rm x}$  film can cycle between a fully oxidized fluorite phase and a partially reduced perovskite phase.

# 3.2. Electron microscopy

STEM images along with EDS maps (of the indicated region) for Al, Ce, and Mn are shown in Figs. 2 and 3 for an oxidized and a reduced  $\text{CeMnO}_x/\gamma\text{-Al}_2\text{O}_3$  sample, respectively. The EDS maps show a close correspondence between the three different elements demonstrating that the  $\text{CeMnO}_x$  film is conformal to the  $\gamma\text{-Al}_2\text{O}_3$  support and remains so after repeated redox cycling at high temperature.

To obtain additional insight into the structure of the CeMnO $_{x}$  film, HRTEM images of both an oxidized and a reduced CeMnO $_{x}/\gamma\text{-Al}_{2}O_{3}$  sample were collected and are displayed in Figs. 4 and 5, respectively. The inset in each image corresponds to the Fourier transform diffractogram of the indicated region. In these images, well-defined lattice fringes are readily apparent. Since such fringes are not observed in the HRTEM image of the bare  $\gamma\text{-Al}_{2}O_{3}$  support due to its low crystallinity, they can be attributed to the CeMnO $_{x}$  thin film.

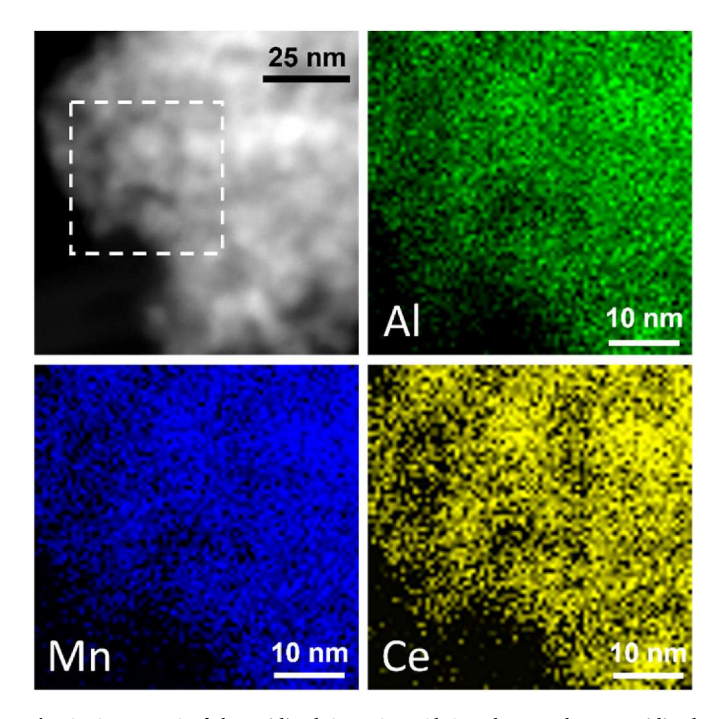


Fig. 2. STEM-EDS of the oxidized CeMnO  $_x/\gamma$  -Al  $_2{\rm O}_3$  . The sample was oxidized in 10% dry air in He at 1073 K.

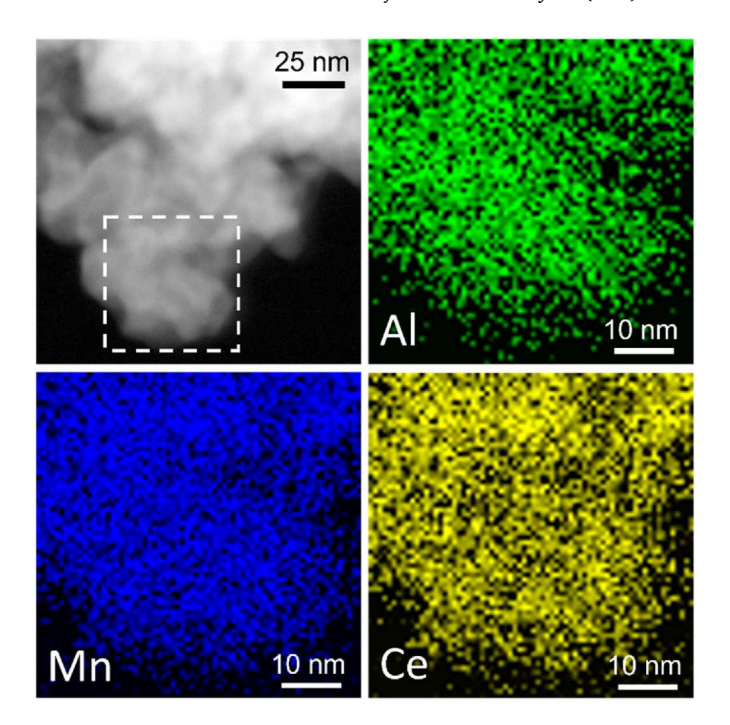


Fig. 3. STEM-EDS of the reduced CeMnO  $_x/\gamma$  -Al  $_2O_3$  . The sample reduced in 10% dry H $_2$  in He at 1073 K.

The lattice fringes in the images of the oxidized sample in Fig. 4a and b can both be indexed to planes in fluorite CeMnO<sub>x</sub> (f-CMO). In particular, those in Fig. 4a correspond to the (-100), (010) and (110) planes near the [001] zone axis and those in Fig. 4b to (200) and (1-31) planes near [013] zone axis. A different set of fringes is observed, however, in the HRTEM image of the reduced sample in Fig. 5a and b. These can be indexed to the (110) plane along the [-111] zone axis (Fig. 5a) and the (100) plane along the [001] zone axis (Fig. 5b) of perovskite CeMnO<sub>x</sub> (p-CMO). These results are consistent with the XRD results which show that the CeMnO<sub>x</sub>/ $\gamma$ -Al<sub>2</sub>O<sub>3</sub> sample can be reversibly cycled between a reduced perovskite phase and an oxidized fluorite phase.

# 3.3. XPS and EELS analysis

The oxidation states of Ce and Mn cations in both the oxidized and the reduced CeMnO $_{\rm x}/\gamma$ -Al $_2$ O $_3$  sample were determined by XPS and EELS. The XPS spectra in Fig. 6a show the Ce(3 $d_{3/2}$ ) and Ce(3 $d_{5/2}$ ) regions for the oxidized and the reduced CeMnO $_{\rm x}/\gamma$ -Al $_2$ O $_3$  samples. The spectrum for the oxidized sample contains three 3 $d_{5/2}$  - 3 $d_{3/2}$  doublets, which are labeled u/v, u"/v" and u"'/v" and are characteristic of Ce<sup>4+</sup> cations [23–25]. The u"'/v"' doublet centered at 917.0 and 898.4 eV is due to the primary photoemission of Ce<sup>4+</sup>, and the u-v and u"'-v" doublets located at 901.2, and 883.0, and at 907.1 and 888.6 eV, respectively, correspond to two separate shake-down satellite features associated with the excitation of one or two electrons from the filled O (2p) orbital to an empty Ce(4f) orbital during photoemission [23,24]. These data show that this CeMnO $_{\rm x}/\gamma$ -Al $_2$ O $_3$  sample contains primarily Ce<sup>4+</sup>.

For the reduced sample, the spectrum is mainly composed of two  $3d_{3/2}$  -  $3d_{5/2}$  doublets, labeled as  $u^0/v^0$  and u'/v', at 903.7 and 885.9 eV, and at 899.0 and 881.1 eV, respectively, which are consistent with that reported previously for  $Ce^{3+}$  [23,24]. In this case the  $u^0/v^0$  doublet are the primary photoemission peaks and the u'/v' doublet is another shake-down feature resulting from the excitation of an electron from the filled O(2p) orbital to an empty Ce(4f) orbital during photoemission. As shown in the figure, small peaks for  $Ce^{4+}$  are also present in this spectrum. Based on the peak areas, it is estimated  $\sim$ 3% of the Ce is in the +4-oxidation state in this sample. It's possible the  $Ce^{4+}$ may be

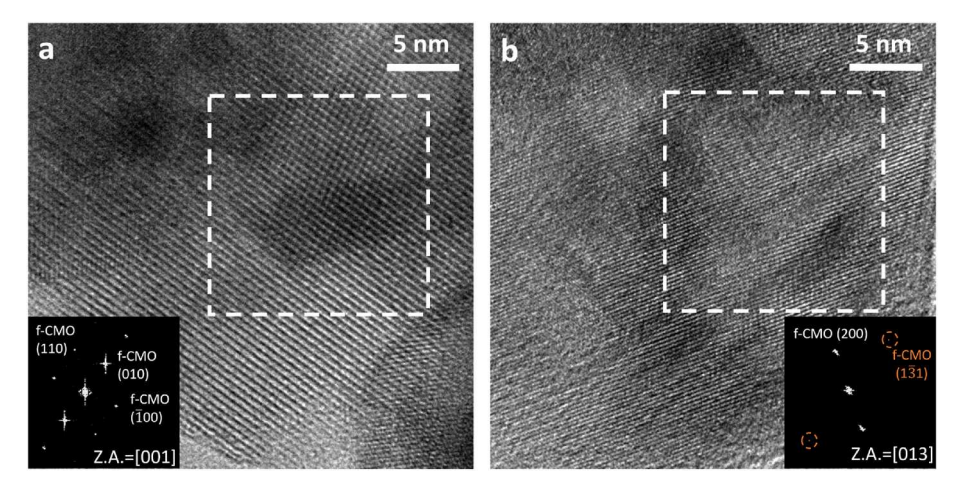


Fig. 4. HRTEM and corresponding FFT diffraction patterns of the indicated areas of the oxidized  $CeMnO_x/\gamma$ - $Al_2O_3$ . The sample was oxidized in 10% dry air in He at 1073 K.

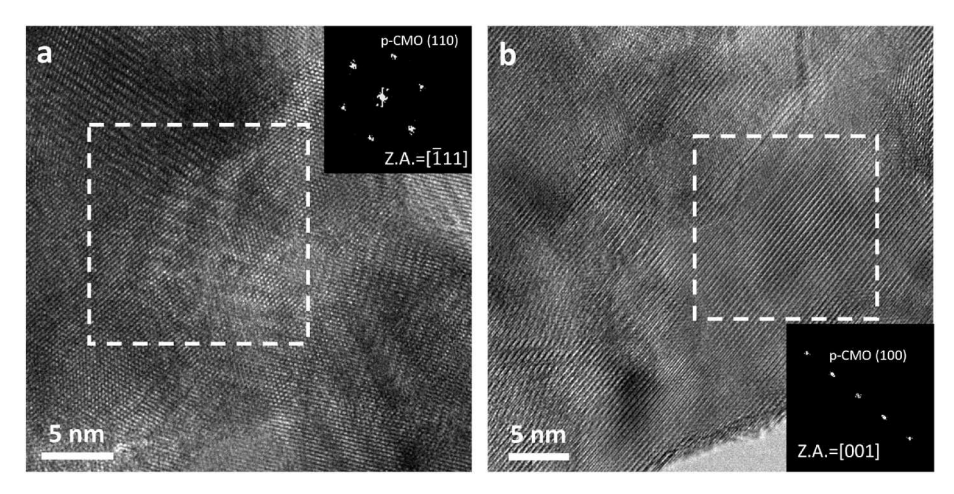


Fig. 5. HRTEM and corresponding FFT diffraction patterns of the indicated areas of the reduced CeMnO $_x/\gamma$ -Al $_2$ O $_3$ . The sample was reduced in 10% H $_2$  in He at 1073 K.

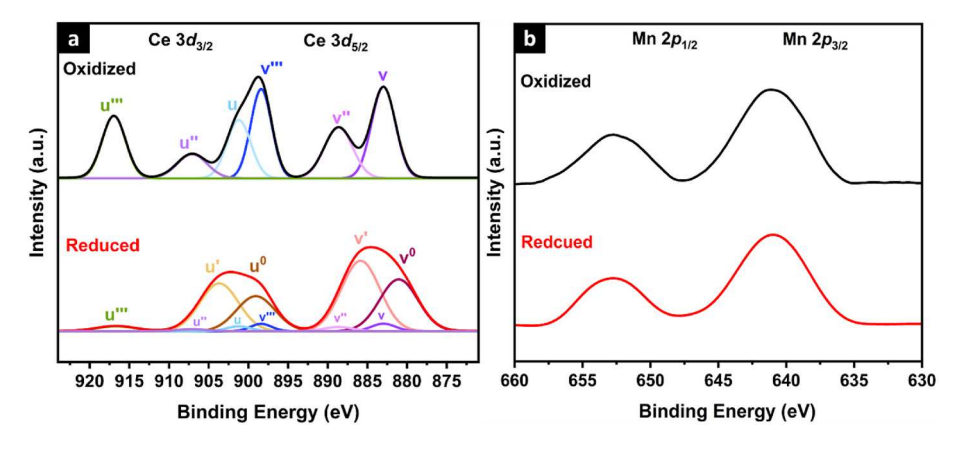


Fig. 6. XPS spectra of (a) Ce  $3d_{3/2}$  and Ce  $3d_{5/2}$  regions and (b) Mn  $2p_{1/2}$  and Mn  $2p_{3/2}$  regions of the oxidized (10% dry air in He at 1073 K) and the reduced (10% H<sub>2</sub> in He at 1073 K) CeMnO<sub>x</sub>/ $\gamma$ -Al<sub>2</sub>O<sub>3</sub> samples.

associated with a small amount of  $CeO_2$  in the sample due to Ce–Mn imbalance caused by the formation of  $MnAl_2O_4$  at the support interface as discussed earlier. Nonetheless, the Ce XPS data shows that the reduced sample contained primarily  $Ce^{3+}$ .

Fig. 6b shows the Mn(2p) region of the XPS spectra for the oxidized and the reduced CeMnO $_x/\gamma$ -Al $_2$ O $_3$  samples. For the oxidized sample, the

spectrum features a  $Mn(2p_{1/2})$  and  $Mn(2p_{3/2})$  doublet centered at 652.6 and 641.1 eV [26]. This spectrum is similar to that reported for  $Mn^{3+}$  in LaMnO<sub>3</sub> perovskite [27]. The Mn(2p) spectrum for the reduced sample was nearly identical to that of the oxidized sample indicating that the Mn remained in the +3-oxidation state.

EELS spectra of Ce  $M_{4,5}$  edges and Mn  $L_{2,3}$  edges for the oxidized and

the reduced CeMnO $_{\rm x}/\gamma$ -Al $_{\rm 2}O_{\rm 3}$  samples are displayed in Fig. 7. The spectrum of the oxidized sample in Fig. 7a shows the Ce  $M_5$  and  $M_4$  edges at 885.0 and 902.8 eV, respectively, which are characteristic of Ce<sup>4+</sup> [28]. However, for the reduced sample, both edges shift to lower energy and appear at 900.4 and 882.8 eV, indicating a change in the Ce oxidation state from +4 to +3 upon reduction [28,29], which is consistent with the XPS results. In Fig. 7b, Mn L $_3$  and  $L_2$  edges are plotted for the oxidized and the reduced CeMnO $_{\rm x}/\gamma$ -Al $_2$ O $_3$  sample. The Mn L $_3$  and  $L_2$  edges for the oxidized sample appear at 641.1 and 652.5 eV, respectively, which are close to those reported for Mn $^3$ + in the perovskite LaMnO $_3$  [30,31]. A similar spectrum was obtained for the reduced sample with both edges remaining at 641.1 and 652.5 eV, indicating that Mn does not undergo redox and remained Mn $^{+3}$  upon redox cycling which is again consistent with the XPS data.

# 3.4. Redox isotherms

CT was used to measure the redox isotherm of the CeMnO $_x/\gamma$ -Al $_2$ O $_3$  sample at 1073 K and is plotted in Fig. 8. For comparison, a previously measured redox isotherm for a 2 nm thick CeFeO $_x/\gamma$ -Al $_2$ O $_3$  thin film sample [11] is also included in the figure. Since the Ce and Mn cations in the oxidized sample were shown by XPS and EELS to be predominantly in the +4- and +3-oxidation states, respectively, the y axis in the plot was calibrated by assuming that the fully oxidized film had a stoichiometry of CeMnO $_3$ .5. This calibration was further verified by the consistency between CT and flow-titration measurements, both of which gave an x value close to 2.9 for the reduced CeMnO $_x/\gamma$ -Al $_2$ O $_3$  sample. Note that the  $\gamma$ -Al $_2$ O $_3$  support is irreducible for the conditions used in the CT measurements and thus will not impact the measurement of the x value of the perovskite film.

The redox isotherm in Fig. 8 contains one distinct step or phase transition at a P(O<sub>2</sub>) of  $10^{-9.5}$  atm, corresponding to an equilibrium between CeMnO<sub>3.5</sub> and CeMnO<sub>3</sub>. This is different from the isotherm for CeFeO<sub>x</sub>/ $\gamma$ -Al<sub>2</sub>O<sub>3</sub> sample, in which there are two steps at P(O<sub>2</sub>) values of  $10^{-8.8}$  atm and  $10^{-15}$  atm, respectively. This difference demonstrates that the Mn<sup>3+</sup> cations in the CeMnO<sub>3</sub> film are stabilized in the perovskite film and cannot be further reduced to a lower oxidation state, while in contrast approximately half of the Fe<sup>3+</sup> cations in the CeFeO<sub>3</sub> film can be reduced to Fe<sup>2+</sup> at a P(O<sub>2</sub>) value of  $10^{-15}$  atm. This result shows that the perovskite CeMnO<sub>3</sub> film has superior redox stability compared to the perovskite CeFeO<sub>3</sub> film. It is noteworthy that the stoichiometry of CeMnO<sub>x</sub>/ $\gamma$ -Al<sub>2</sub>O<sub>3</sub> sample decreases gradually from CeMnO<sub>3</sub> to CeMnO<sub>2.9</sub> with further reduction. This may be the result of a small fraction of Mn<sup>3+</sup> near the  $\gamma$ -Al<sub>2</sub>O<sub>3</sub> surface being reduced to Mn<sup>2+</sup> due to reaction with the support and is consistent with the observation of a small amount of MnAl<sub>2</sub>O<sub>4</sub> in the XRD pattern for the reduced CeMnO<sub>x</sub>/ $\gamma$ -Al<sub>2</sub>O<sub>3</sub> sample.

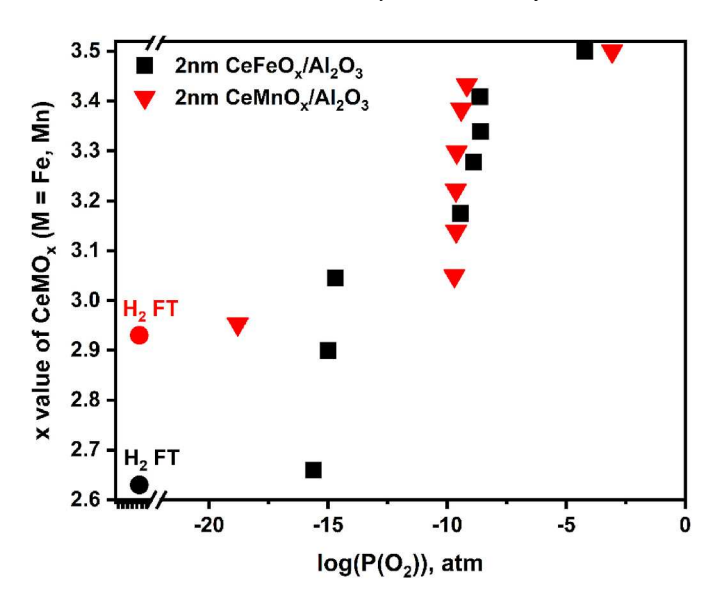
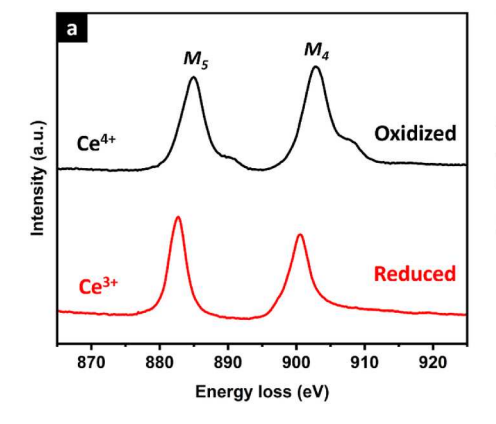


**Fig. 8.** CT redox isotherms for CeMnO<sub>x</sub>/ $\gamma$ -Al<sub>2</sub>O<sub>3</sub> (red solid triangles) and CeFeO<sub>x</sub>/ $\gamma$ -Al<sub>2</sub>O<sub>3</sub> at 1073 K (black solid squares). The oxygen stoichiometry of the 10% hydrogen-reduced CeMnO<sub>x</sub>/ $\gamma$ -Al<sub>2</sub>O<sub>3</sub> sample (red solid circle) and CeFeO<sub>x</sub>/ $\gamma$ -Al<sub>2</sub>O<sub>3</sub> sample (black solid circle) are also shown in the figure which were measured by flow titration (FT).

# 4. Discussion

As discussed in the introduction, Ce<sup>3+</sup> has been reported to form CeMO<sub>3</sub> perovskite phases only with V, Cr and Fe M-site cations. While there are a few reports in the literature claiming the formation of CeMnO<sub>3</sub>, the XRD results in these studies suggest that the samples predominantly had a fluorite structure with only a minority perovskite phase. It is also noteworthy that CeCrO3 and CeFeO3, which can be synthesized as single-phase perovskites [10,32], irreversibly phase-separate into CeO<sub>2</sub> and a second oxide phase upon high-temperature oxidation or redox cycling [11,33]. In contrast to these observations, in the present study we have demonstrated the ALD growth of a single phase, conformal thin film of perovskite CeMnO<sub>3</sub> on a high surface area γ-Al<sub>2</sub>O<sub>3</sub> support. Furthermore, cycling the CeMnO<sub>3</sub> thin film between reducing and oxidizing conditions did not induce irreversible separation into two oxide phases, as observed for the bulk Ce-containing perovskite oxides. This indicates that interactions between the  $CeMnO_x$  and the  $\gamma$ -Al<sub>2</sub>O<sub>3</sub> help stabilize the structure of the thin film, especially under oxidizing conditions at high temperature.

The oxidized  $CeMnO_x$  thin film was shown by XPS and EELS to contain  $Ce^{+4}$  and  $Mn^{+3}$ . The XRD pattern for this material only



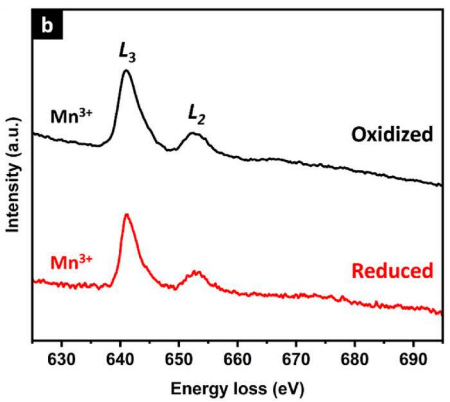


Fig. 7. EELS spectra of (a) Ce  $M_{4,5}$  edges and (b) Mn  $L_{2,3}$  edges for the oxidized (10% dry air in He at 1073 K) and the reduced (10%  $H_2$  in He at 1073 K) CeMnO<sub>x</sub>/ $\gamma$ -Al<sub>2</sub>O<sub>3</sub> sample.

contained peaks indicative of a fluorite-structured oxide. This coupled with the lack of XRD peaks for  $MnO_x$  species suggests that at least some of the  $Mn^{3+}$  cations were substituted for  $Ce^{4+}$  in the  $CeO_2$  fluorite lattice. It is unlikely, however, that all of the  $Mn^{3+}$  could be accommodated in this way, since it would require an unusually high concentration of oxygen vacancies to maintain charge neutrality. It is possible, however, that in addition to partial substation into the fluorite lattice,  $Mn^{3+}$  cations occupy interstitial sites, as has been proposed by Murugan et al. in their study of  $Ce_{1-x}Mn_xO_{2-d}$  solid solutions [34]. A similar model had also been applied by Li et al. to account for the high  $Fe^{3+}$  dopant content in  $Ce_{1-x}Fe_xO_2$  solid solutions [35].

In addition to a higher phase stability than the bulk material, the CeMnO<sub>x</sub> film had interesting thermodynamic properties. At 1073 K the Ce<sup>4+</sup> cations in the fully oxidized CeMnO<sub>3.5</sub> film underwent reduction to  $Ce^{3+}$  at a P(O<sub>2</sub>) of  $10^{-9.5}$  atm, resulting in the formation of the CeMnO<sub>3</sub> perovskite phase (Figs. 6–8). It is noteworthy that this result is opposite to what one would predict based on the thermodynamic properties of the individual binary oxides which indicate that Mn<sup>3+</sup> should be significantly easier to reduce than  $Ce^{4+}$ . For example, the  $\Delta G$  of reductions for the bulk oxides predict that at 1073 K reduction of CeO<sub>2</sub> to  $Ce_2O_3$  ( $Ce^{4+} \rightarrow Ce^{3+}$ ) and reduction of  $Mn_3O_4$  to MnO ( $Mn^{3+} \rightarrow Mn^{2+}$ ) would occur at  $P(O_2)$  values of  $10^{-22}$  atm and  $10^{-9}$  atm, respectively. This result is similar to what we have observed previously for CeFeO<sub>x</sub> thin films on  $\gamma$ -Al<sub>2</sub>O<sub>3</sub> where the transition of fluorite CeFeO<sub>3,5</sub> to perovskite CeFeO<sub>3</sub> at 1073 K occurs at a  $P(O_2)$  of  $10^{-8}$  atm and involves only the reduction of Ce<sup>4+</sup> to Ce<sup>3+</sup> (see Fig. 8) with the ostensibly more reducible Fe cations remaining in the +3-oxidation state [11]. Together these results demonstrate that the perovskite structure greatly enhances the stability of the B site Mn and Fe cations.

While it was observed that the  $Ce^{4+}$  undergoes reduction prior to the B site cation in both  $CeMnO_x$  and  $CeFeO_x$  thin films, the CT data in Fig. 8 shows that there are still some differences in the redox properties for these materials. Most notably, for  $CeFeO_x/\gamma-Al_2O_3$  after the initial reduction of  $Ce^{4+}$  to  $Ce^{3+}$  there is a second step at a  $P(O_2)$  of  $P(O_2)$  at the which corresponds to reduction of a portion of the  $P(O_2)$  at the initial reduction steps for  $P(O_2)$  s between  $P(O_2)$  s between  $P(O_2)$  s between  $P(O_2)$  s between  $P(O_2)$  and  $P(O_2)$  at low as  $P(O_2)$  at the ceMnOx films do not undergo reduction at  $P(O_2)$  as low as  $P(O_2)$  at the since as noted above, reduction of  $P(O_2)$  in bulk  $P(O_2)$  at much higher  $P(O_2)$ .

The redox properties of the  $CeMnO_x$  thin film observed here make it an interesting candidate for use in applications ranging from high-temperature electrocatalysis, to supports for metal catalysts, to oxygen storage media for chemical looping reaction systems [36,37]. The low surface areas obtained for the bulk material and its propensity to separate into multiple oxide phases upon redox cycling have limited its use in these applications. The results obtained in this study show that these limitations may be overcome using ALD to grow a conformal film of  $CeMnO_x$  on  $\gamma$ -Al<sub>2</sub>O<sub>3</sub> to produce a material with a relatively high surface area. It was demonstrated that oxygen could be reversibly added or removed from a  $CeMnO_x$  film produced in this manner allowing it to be cycled between perovskite  $CeMnO_3$  and fluorite  $CeMnO_{3.5}$  without separation into separate oxide phases as is observed for bulk  $CeMnO_x$ .

The more accessible  $Ce^{4+}/Ce^{3+}$  redox couple in the  $CeMnO_x$  film compared to  $CeO_2$  along with its high surface area could potentially be exploited in chemical looping processes where an energy-intensive high-temperature reduction step is required [38]. The ease of reduction of  $Ce^{4+}$  in the  $CeMnO_x$  film would lower this temperature which could enhance the energy efficiency of the process. The redox properties of the  $CeMnO_3$  film may also make it a good support and promoter for metal catalysts, especially for oxidation and selective oxidation reactions in which the oxide can enhance the metal activity through transfer of oxygen from the oxide to the metal [39,40]. This is something that we plan to investigate in future studies.

#### 5. Conclusions

In this study, we have examined the properties of a conformal film of cerium-manganese mixed oxide, CeMnO<sub>x</sub>, on a high surface area γ-Al<sub>2</sub>O<sub>3</sub> support that was grown by ALD. The CeMnO<sub>x</sub> film formed a perovskite phase after reduction in H2 at 1073 K, in which both the Ce and Mn cations are predominantly in the +3-oxidation state. At  $P(O_2)$  values as low as  $10^{-19}$  atm. Mn cations in the film remained in the +3-oxidation state and were not reduced to lower oxidation states at this temperature as is observed in bulk manganese oxide. This demonstrates that the perovskite structure of the CeMnO<sub>3</sub> film stabilizes the Mn<sup>3+</sup> cations. Upon oxidation in air, a fluorite phase was formed with a stoichiometry of CeMnO<sub>3,5</sub> and Ce<sup>3+</sup> cations were oxidized to Ce<sup>4+</sup> at a P(O<sub>2</sub>) of  $10^{-9}$ atm at 1073 K, which is much higher than that observed for oxidation of Ce<sup>3+</sup> to Ce<sup>4+</sup> in bulk ceria. This again can be attributed to the stability of the perovskite CeMnO3 lattice which stabilized both the Ce and Mn cations in the +3-oxidation state. The reversibility of the above phase transition between an oxidized fluorite CeMnO<sub>3.5</sub> and a reduced perovskite CeMnO<sub>3</sub> was demonstrated by redox cycling of this material at elevated temperatures. The conformal nature of the film was also maintained during repeated redox cycling.

#### CRediT authorship contribution statement

Kai Shen: Data curation, Formal analysis, Investigation, Writing. Mengjie Fan: Data curation, Formal analysis, Investigation. Rajeev Kumar Rai: Data curation, Formal analysis, Investigation. Eric A. Stach: Supervision. Raymond J. Gorte: Supervision, Supervision, Writing. John M. Vohs: Supervision, Supervision, Writing.

# **Declaration of competing interest**

The authors declare the following financial interests/personal relationships which may be considered as potential competing interests: John M. Vohs reports was provided by University of Pennsylvania, Department of Chemical and Biomolecular Engineering. John M. Vohs reports financial support was provided by Air Force Office of Scientific Research.

#### Data availability

Data will be made available on request.

#### Acknowledgements

This work was supported by the Air Force Office of Scientific Research, under AFOSR Award No. FA9550-19-1-0326. Some of the work was performed at the Singh Center for Nanotechnology at the University of Pennsylvania, a member of the National Nanotechnology Coordinated Infrastructure (NNCI) network, which is supported by the National Science Foundation (Grant NNCI-2025608). The authors also gratefully acknowledge support of the Nanoscale Characterization Facility at the Singh Center by the NSF through the University of Pennsylvania Materials Research Science and Engineering Center (MRSEC) (DMR-1720530).

# References

- M. Sugiura, M. Ozawa, A. Suda, T. Suzuki, T. Kanazawa, Development of innovative three-way catalysts containing ceria-zirconia solid solutions with high oxygen storage/release capacity, Bull. Chem. Soc. Jpn. 78 (2005) 752–767.
- [2] M. Mogensen, N.M. Sammes, G.A. Tompsett, Physical, chemical and electrochemical properties of pure and doped ceria, Solid State Ionics 129 (2000) 63–94
- [3] T. Kim, J.M. Vohs, R.J. Gorte, Thermodynamic investigation of the redox properties of ceria-zirconia solid solutions, Ind. Eng. Chem. Res. 45 (2006) 5561–5565.

- [4] P.R. Shah, T. Kim, G. Zhou, P. Fornasiero, R.J. Gorte, Evidence for entropy effects in the reduction of ceria-zirconia solutions, Chem. Mater. 18 (2006) 5363–5369.
- [5] K. Eguchi, T. Setoguchi, T. Inoue, H. Arai, Electrical-properties of ceria-based oxides and their application to solid oxide fuel-cells, Solid State Ionics 52 (1992) 165–172.
- [6] R.J. Gorte, Ceria in catalysis: from automotive applications to the water gas shift reaction, AIChE J. 56 (2010) 1126–1135.
- [7] A. Trovarelli, Catalytic properties of ceria and CeO2-containing materials, Catal. Rev. Sci. Eng. 38 (1996) 439–520.
- [8] M. Yoshimura, T. Sata, A new monoclinic phase of cerium orthovanadate (CeVO<sub>4</sub>), Bull. Chem. Soc. Jpn. 42 (1969) 3195–3198.
- [9] R.F. Reidy, K.E. Swider, Determination of the cerium oxidation-state in cerium vanadate, J. Am. Ceram. Soc. 78 (1995) 1121–1122.
- [10] M. Robbins, G.K. Wertheim, A. Menth, R.C. Sherwood, Preparation and properties of polycrystalline cerium orthoferrite (CeFeO3), J. Phys. Chem. Solid. 30 (1969) 1823–1825.
- [11] K. Shen, M.J. Fan, O. Kwon, A.J. Viescas, G.C. Papaefthymiou, R.J. Gorte, J. M. Vohs, Reversible perovskite-fluorite phase transition in alumina-supported CeFeO<sub>x</sub> films, J. Mater. Chem. (2023), https://doi.org/10.1039/d2ta06215a. Advance Article.
- [12] X. Liu, X.Y. Lv, Y.Q. Wang, C.C. Zhao, F. Liu, Effect of calcination process on performance of 3DOM CeMnO3 catalysts, J. Rare Earths 39 (2021) 1073–1081.
- [13] Q.L. Hu, B. Yue, F. Yang, H.Y. Shao, J.H. Wang, L. Ji, Y.F. Jia, Y. Wang, J.H. Liu, Facile synthesis and electrochemical properties of perovskite-type CeMnO3 nanofibers, ChemistrySelect 4 (2019) 11903–11912.
- [14] H.H. Yi, J.L. Xu, X.L. Tang, S.Z. Zhao, Y.Y. Zhang, Z.Y. Yang, J.M. Wu, X.M. Meng, J.X. Meng, H. Yan, Q. Li, Novel synthesis of Pd-CeMnO<sub>3</sub> perovskite based on unique ultrasonic intervention from combination of Sol-Gel and impregnation method for low temperature efficient oxidation of benzene vapour, Ultrason. Sonochem. 48 (2018) 418–423.
- [15] H.S. Anusha, S. Yadav, T. Tenzin, J.S. Prabagar, K.M. Anilkumar, W. Kitirote, H. P. Shivaraju, Improved CeMnO3 perovskite framework for visible-light-aided degradation of tetracycline hydrochloride antibiotic residue and methylene blue dye, Int. J. Environ. Sci. Technol. (2022), https://doi.org/10.1007/s13762-022-04742-3.
- [16] G. Zhou, P.R. Shah, R.J. Gorte, A study of cerium-manganese mixed oxides for oxidation catalysis. Catal. Lett. 120 (2008) 191–197.
- [17] A.A. Belik, L. Zhang, N. Terada, Y. Katsuya, M. Tanaka, Y. Matsushita, K. Yamaura, A-site-ordered quadruple perovskite manganite CeMn<sub>7</sub>O<sub>12</sub> with trivalent cations, J. Solid State Chem. 283 (2020) 121161–121169.
- [18] T.M. Onn, S.Y. Zhang, L. Arroyo-Ramirez, Y. Xia, C. Wang, X.Q. Pan, G.W. Graham, R.J. Gorte, High-surface-area ceria prepared by ALD on Al<sub>2</sub>O<sub>3</sub> support, Appl. Catal., B 201 (2017) 430–437.
- [19] I. Baldychev, R.J. Gorte, J.M. Vohs, The impact of redox properties on the reactivity of  $V_2O_5/Al_2O_3$  catalysts, J. Catal. 269 (2010) 397–403.
- [20] B.M. Reddy, K.N. Rao, G.K. Reddy, A. Khan, S.E. Park, Structural characterization and oxidehydrogenation activity of CeO<sub>2</sub>/Al<sub>2</sub>O<sub>3</sub> and V<sub>2</sub>O<sub>5</sub>/CeO<sub>2</sub>/Al<sub>2</sub>O<sub>3</sub> catalysts, J. Phys. Chem. C 111 (2007) 18751–18758.
- [21] M.M. Natile, G. Boccaletti, A. Glisenti, Properties and reactivity of nanostructured CeO<sub>2</sub> powders: comparison among two synthesis procedures, Chem. Mater. 17 (2005) 6272–6286.

- [22] H.F. Li, G.Z. Lu, Q.G. Dai, Y.Q. Wang, Y. Guo, Y.L. Guo, Efficient low-temperature catalytic combustion of trichloroethylene over flower-like mesoporous Mn-doped GeO<sub>2</sub> microspheres, Appl. Catal., B 102 (2011) 475–483.
- [23] D.A. Creaser, P.G. Harrison, M.A. Morris, B.A. Wolfindale, X-ray Photoelectron spectroscopic study of the oxidation and reduction of a cerium(III) oxide cerium foil substrate, Catal. Lett. 23 (1994) 13–24.
- [24] A. Pfau, K.D. Schierbaum, The electronic-structure of stoichiometric and reduced CeO<sub>2</sub> surfaces - an XPS, UPS and HREELS study, Surf. Sci. 321 (1994) 71–80.
- [25] A. Pfau, K.D. Schierbaum, W. Gopel, The electronic-structure of CeO<sub>2</sub> thin-films the influence of Rh surface dopants, Surf. Sci. 331 (1995) 1479–1485.
- [26] E.S. Ilton, J.E. Post, P.J. Heaney, F.T. Ling, S.N. Kerisit, XPS determination of Mn oxidation states in Mn (hydr)oxides, Appl. Surf. Sci. 366 (2016) 475–485.
- [27] J.H. Chen, M.Q. Shen, X.Q. Wang, G.S. Qi, J. Wang, W. Li, The influence of nonstoichiometry on LaMnO<sub>3</sub> perovskite for catalytic NO oxidation, Appl. Catal., B 134 (2013) 251–257.
- [28] L.A.J. Garvie, P.R. Buseck, Determination of Ce4+/Ce3+ in electron-beam-damaged CeO<sub>2</sub> by electron energy-loss spectroscopy, J. Phys. Chem. Solid. 60 (1999) 1943–1947.
- [29] A.M. D'Angelo, A.C.Y. Liu, A.L. Chaffee, Oxygen uptake of Tb-CeO<sub>2</sub>: analysis of Ce<sup>3</sup> and oxygen vacancies, J. Phys. Chem. C 120 (2016) 14382–14389.
- [30] J. Verbeeck, O.I. Lebedev, G. Van Tendeloo, B. Mercey, SrTiO<sub>3</sub>(100)/ (LaMnO<sub>3</sub>)<sub>m</sub>(SrMnO<sub>3</sub>)<sub>n</sub> layered heterostructures: a combined EELS and TEM study, Phys. Rev. B 66 (2002) 184426–184435.
- [31] Z.H. Chen, Z.H. Chen, Z.Q. Liu, M.E. Holtz, C.J. Li, X.R. Wang, W.M. Lu, M. Motapothula, L.S. Fan, J.A. Turcaud, L.R. Dedon, C. Frederick, R.J. Xu, R. Gao, A.T. N'Diaye, E. Arenholz, J.A. Mundy, T. Venkatesan, D.A. Muller, L.W. Wang, J. Liu, L.W. Martin, Electron accumulation and emergent magnetism in LaMnO<sub>3</sub>/SrTiO<sub>3</sub> heterostructures, Phys. Rev. Lett. 119 (2017) 156801–156807.
- [32] R. Shukla, A.K. Bera, S.M. Yusuf, S.K. Deshpande, A.K. Tyagi, W. Hermes, M. Eul, R. Pottgen, Multifunctional nanocrystalline CeCrO<sub>3</sub>: antiferromagnetic, relaxor, and optical properties, J. Phys. Chem. C 113 (2009) 12663–12668.
- [33] S. Bensaid, G.A. Blengini, D. Fino, N. Russo, Diesel soot combustion with A<sub>1-x</sub>A<sub>x</sub>'B<sub>1</sub>.

  <sub>v</sub>B<sub>v</sub>'O<sub>3+8</sub> perovskite catalysts, Chem. Eng. Commun. 201 (2014) 1327–1339.
- [34] B. Murugan, A.V. Ramaswamy, D. Srinivas, C.S. Gopinath, V. Ramaswamy, Nature of manganese species in Ce<sub>1-x</sub>Mn<sub>x</sub>O<sub>2-8</sub> solid solutions synthesized by the solution combustion route, Chem. Mater. 17 (2005) 3983–3993.
- [35] G.S. Li, R.L. Smith, H. Inomata, Synthesis of nanoscale Ce<sub>1-x</sub>Fe<sub>x</sub>O<sub>2</sub> solid solutions via a low-temperature approach, J. Am. Chem. Soc. 123 (2001) 11091–11092.
- [36] X.F. Tang, J.L. Chen, X.M. Huang, Y. Xu, W.J. Shen, Pt/MnO<sub>x</sub>-CeO<sub>2</sub> catalysts for the complete oxidation of formaldehyde at ambient temperature, Appl. Catal., B 81 (2008) 115–121.
- [37] M. Johansson, T. Mattisson, A. Lyngfelt, Investigation of Mn<sub>3</sub>O<sub>4</sub> with stabilized ZrO<sub>2</sub> for chemical-looping combustion, Chem. Eng. Res. Des. 84 (2006) 807–818.
- [38] L. Zeng, Z. Cheng, J.A. Fan, L.S. Fan, J.L. Gong, Metal oxide redox chemistry for chemical looping processes, Nat. Rev. Chem 2 (2018) 349–364.
- [39] G.S. Qi, R.T. Yang, R. Chang, MnO<sub>x</sub>-CeO<sub>2</sub> mixed oxides prepared by coprecipitation for selective catalytic reduction of NO with NH<sub>3</sub> at low temperatures, Appl. Catal., B 51 (2004) 93–106.
- [40] H. Wang, H. Zhou, S.Q. Li, X. Ge, L. Wang, Z. Jin, C.T. Wang, J.B. Ma, X.F. Chu, X. J. Meng, W. Zhang, F.S. Xiao, Strong oxide-support interactions accelerate selective dehydrogenation of propane by modulating the surface oxygen, ACS Catal. 10 (2020) 10559–10569.